Received: 8 July 2019 | Revised: 26 September 2019 | Accepted: 8 October 2019

DOI: 10.1111/jace.16843

Journal of the American Ceramic Society

ORIGINAL ARTICLE

The grain-boundary resistance of CeO_2 ceramics: A combined microscopy-spectroscopy-simulation study of a dilute solution

Jana P. Parras[1] | Chen Cao[2] | Zheng Ma[3] | Robert Mücke[2] | Lei Jin[3] | Rafal Dunin-Borkowski[3] | Olivier Guillon[2] | Roger A. De Souza[1]

[1]Institute of Physical Chemistry, RWTH Aachen University, Aachen, Germany

[2]Institute of Energy and Climate Research (IEK-1), Materials Synthesis and Processing, Forschungszentrum Jülich GmbH, Jülich, Germany

[3]Ernst Ruska-Centre for Microscopy and Spectroscopy with Electrons and Peter Grünberg Institute, Forschungszentrum Jülich GmbH, Jülich, Germany

Correspondence
Jana P. Parras, Institute of Physical Chemistry, RWTH Aachen University, 52056 Aachen, Germany.
Email: parras@pc.rwth-aachen.de

Funding information
Deutsche Forschungsgemeinschaft, Grant/Award Number: DU 1086/10-1, GU 993/9-1 and SO 499/9-1

Abstract

Weakly acceptor-doped ceria ceramics were characterized structurally and compositionally with advanced transmission electron microscopy (TEM) techniques and electrically with electrochemical impedance spectroscopy (EIS). The grain boundaries studied with TEM were found to be free of second phases. The impedance spectra, acquired in the range $703 \leq T/\mathrm{K} \leq 893$ in air, showed several arcs that were analyzed in terms of bulk, grain-boundary, and electrode responses. We ascribed the grain-boundary resistance to the presence of space-charge layers. Continuum-level simulations were used to calculate charge-carrier distributions (of acceptor cations, oxygen vacancies, and electrons) in these space-charge layers. The acceptor cations were assumed to be mobile at high (sintering) temperatures but immobile at the temperatures of the EIS measurements. Space-charge formation was assumed to be driven by the segregation of oxygen vacancies to the grain-boundary core. Comparisons of data from the simulations and from the EIS measurements yielded space-charge potentials and the segregation energy of vacancies to the grain-boundary core. The space-charge potentials from the simulations are compared with values obtained by applying the standard, analytical (Mott–Schottky and Gouy–Chapman) expressions. The importance of modelling space-charge layers from the thermodynamic level is demonstrated.

1 | INTRODUCTION

The internal interfaces termed grain boundaries (GBs) have long been known to lower the oxide-ion conductivity of CeO_2-based ceramics.[1–9] Whereas early studies identified an intergranular siliceous phase as the origin of the diminished conductivity, later studies revealed that even pristine GBs, that is, those free of intergranular phases, exhibited a substantially lower conductivity. This effect was attributed to the presence of space-charge layers (SCLs) that are depleted of the predominant mobile charge carriers, oxygen vacancies.[9–13]

To date, the vast majority of work on GBs in ceria has been performed on concentrated solid solutions, M_2O_3–CeO_2. This is due to such compositions displaying the highest oxide-ion conductivities, and the driving force behind the research has been optimizing the ionic conductivity of CeO_2-based ceramics, so that they can be used as electrolytes in solid oxide fuel cells (SOFC). Such solid solutions, however, constitute materials systems in which defect–defect interactions are evidently important.[14–17] The analysis of the SCLs at the GBs of such concentrated solid solutions, on the other hand, has been based on the

dilute-solution approximation (Poisson–Boltzmann ansatz), in which defect–defect interactions are neglected. This discrepancy will lead necessarily to inconsistencies and errors.[18,19]

The attraction of the dilute-solution approximation is that analytical solutions for the GB resistance can be derived for two extreme, simple cases: (a) the Mott–Schottky case, for which the dopant concentration is constant in the SCLs (Figure 1A); and (b) the Gouy–Chapman case, for which the dopant accumulation profile is in electrochemical equilibrium (Figure 1B). For concentrated solid solutions, neither Mott–Schottky nor Gouy–Chapman is appropriate,[19] but even in the dilute case both approaches do not constitute a correct description of SCLs in ceria samples. Ceria is characterized, namely, by dopant cations that are mobile at high (sintering) temperatures but immobile at the (lower) temperatures of the impedance measurements. The dopant accumulation profile will be frozen in, therefore, from some critical temperature (T_{crit}) below which the dopant cations are insufficiently mobile (at the given cooling rate) to achieve electrochemical equilibrium. In the literature, experimental resistance data are usually analyzed in terms of the Mott–Schottky case, even though the dopant concentration is not constant.[9,20–29]

In this study, we take a dilute solution of Y-doped CeO_2, and we analyze the GBs experimentally with transmission electron microscopy (TEM) and with electrochemical impedance spectroscopy (EIS). Furthermore, we perform continuum-level simulations with finite-element-method (FEM) calculations to provide a description of point-defect concentrations at GBs, and thus, of the GB resistance, that is much closer to reality. That is, the acceptor dopants are allowed to equilibrate at some (high) critical temperature, but their accumulation profiles are kept frozen-in at the temperatures of the impedance studies (Figure 1C). The oxygen vacancies are considered to be mobile at all temperatures.

2 | EXPERIMENTAL PROCEDURE

2.1 | Sample preparation

CeO_2 powder doped with 0.11 mol% Y was obtained commercially (CerPoTech), with an average primary particle size of (22.2 ± 0.5) nm. X-ray powder diffraction indicated that the powder is single phase, fluorite-structured CeO_2. According to ICP-OES measurements, the main impurities are Zr (0.19 mol%), P (0.05 mol%), Ca (0.04 mol%), and Si (0.03 mol%). Since Zr is isovalent with Ce, since we do not know if P will be incorporated into the lattice and since Si has a negligible solubility, the composition as far as this study is concerned is thus $Ce_{0.9985}Y_{0.0011}Ca_{0.0004}O_{1.99905}$. The powder was pressed uniaxially at 100 MPa for 2 minutes to give a pellet of (13.01 ± 0.01) mm in diameter and (3.01 ± 0.01) mm in height [this gives a green density of (52.2 ± 0.6)%]. The pellets were sintered at $T_{sint} = 1573$ K in air for 2 hours, after which they were cooled at 30 K min^{-1} to room temperature. Samples were first mechanically ground with SiC paper down to 1200 grit and then polished with colloidal silica suspension to a 50 nm finish. The densities of the sintered samples, determined according to Archimedes' principle, were 94%-96% of the theoretical density.

2.2 | Microstructure analysis

Scanning electron microscopy (SEM) investigations, with a Zeiss Ultra55, were performed on samples that had been polished and then thermally etched (for 90 minutes at 100 K below the sintering temperature). The grain size l^{gr} was calculated by applying a grain segmentation method to a series of SEM images; the analySIS pro software was used with a correction factor of 1.6,[30] that gives the average 3D grain size from the mean 2D grain size.

An electron-transparent specimen for scanning transmission electron microscopy (STEM) was prepared by focussed ion beam (FIB) machining. A Fischion NanoMill 1040 system was used for further polishing, in order to minimize the extent

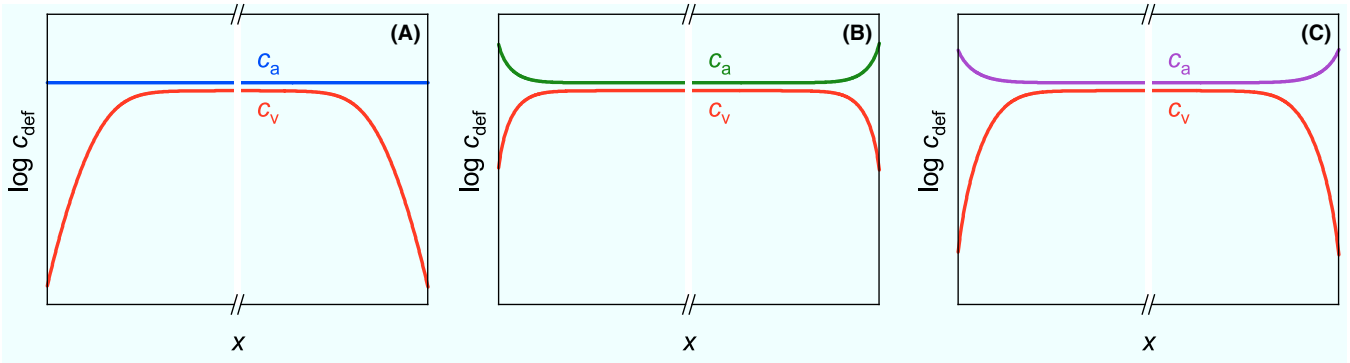

FIGURE 1 Point-defect concentrations across a grain of an ionic solid containing acceptor-dopant cations and charge compensating oxygen vacancies (red lines) at the measurement temperature T_{meas} (electrons are ignored for simplicity). Three different space-charge situations are shown: (A) the Mott–Schottky case, in which the dopant concentration (blue line) is constant across the entire grain; (B) the Gouy–Chapman case, in which the acceptor dopant is accumulated in the SCLs (green line); and (C) a restricted-equilibrium case, in which the dopant accumulation profile (purple) is frozen-in from the critical temperature T_{crit} ($T_{meas} < T_{crit}$)

of the surface damage layers. The final specimen thickness was less than 100 nm. An FEI Titan G^2 80-200 ChemiSTEM microscope, equipped with a spherical aberration corrector for the probe forming system, was employed for the structural characterization. The special resolution is better than 80 pm at the working acceleration voltage of 200 kV. High-angle annular dark-field (HAADF) STEM images were recorded in order to provide information on the GB interfaces. By means of energy-dispersive X-ray spectroscopy (EDXS) mapping, the elemental distribution at/near GB areas were determined.

2.3 | Electrochemical impedance spectroscopy

Two samples, mechanically ground to a thickness of 1.60 mm (sample a) or 1.02 mm (sample b), were studied. Pt|Ag electrodes were used for both specimens: a sample's surface was first sputtered with Pt for 150 seconds (Pt was used to improve the contact), after which Ag paint was applied; the samples were then annealed at 823 K for 1 hour. The electrodes are about 1 mm thick.

Impedance measurements were made on an Alpha-A High Performance Modular Measurement System (Novocontrol Technologies) in the frequency range of $0.1 \leq f/\mathrm{Hz} \leq 4 \times 10^7$ with an amplitude of 30 mV in air in the temperature range $703 \leq T_{\mathrm{meas}}/\mathrm{K} \leq 893$. The resistances and capacities were extracted from the impedance spectra by fitting standard equivalent circuits to the data with the ZView program (version 3.5d, Scribner Associates, Inc).

The specific bulk conductivity was calculated from the bulk resistance R^{b}, sample thickness l^{s}, and sample cross-sectional area A according to

$$\sigma^{\mathrm{b}} = \frac{l^{\mathrm{s}}}{A \cdot R^{\mathrm{b}}}. \tag{1}$$

The resistances of the single GBs are considered to be connected in series, so that the total GB resistance R^{gb} can be converted into the specific GB conductivity through:

$$\sigma^{\mathrm{gb}} = \frac{l^{\mathrm{s}}}{l^{\mathrm{gr}}} \frac{l^{\mathrm{gb}}}{A \cdot R^{\mathrm{gb}}} \tag{2}$$

where l^{gb} is the GB thickness (ie, the thickness of the GB core plus the extension of the SCL on either side of the core). Assuming the dielectric permittivity of grain and GB to be the same, we can relate the ratio $l^{\mathrm{gb}}/l^{\mathrm{gr}}$ to the ratio of the bulk to GB capacitances:

$$\frac{C^{\mathrm{b}}}{C^{\mathrm{gb}}} = \frac{l^{\mathrm{gb}}}{l^{\mathrm{gr}}}. \tag{3}$$

In order to compare the measured EIS data with the simulation results, we use the ratio $\sigma^{\mathrm{b}}/\sigma^{\mathrm{t}}$, with total conductivity $\sigma^{\mathrm{t}} = l^{\mathrm{s}} / \left(A \cdot \left(R^{\mathrm{b}} + R^{\mathrm{gb}}\right)\right)$:

$$\frac{\sigma^{\mathrm{b}}}{\sigma^{\mathrm{t}}} = \frac{R^{\mathrm{gb}}}{R^{\mathrm{b}}} + 1. \tag{4}$$

3 | CONTINUUM SIMULATIONS

3.1 | Bulk-defect chemistry

There is widespread agreement concerning the defect chemistry of bulk CeO_2. Experimental[31–36] and computational[37,38] studies indicate that the electroneutrality condition for acceptor-doped CeO_2 can be approximated well for a wide range of conditions as follows:

$$2c_{\mathrm{v}} = c_{\mathrm{a}} + c_{\mathrm{e}} \tag{5}$$

with c_{v}, c_{a}, and c_{e} being the concentrations of doubly-charged oxygen vacancies, of acceptor dopants ($c_{\mathrm{a}} = c_{\mathrm{Y}} + 2c_{\mathrm{Ca}}$) and of electrons, respectively. (Under very reducing conditions, singly-charged oxygen vacancies, and even neutral oxygen vacancies, have to be taken into account, but in our study we remain in the oxidizing regime and so both these species can be safely neglected.) For the dilute regime ($c_{\mathrm{a}} < 1\%$), we also neglect defect–defect interactions.[14–17,19] We note that the electrons are localized on Ce^{4+} ions as small polarons, forming Ce^{3+} ions. This does not affect the electroneutrality condition [Equation (5)], but it does specify the number of sites available to the electrons (see below).

Experimental and computational studies also indicate that the most important defect reaction in acceptor-doped CeO_2 is the reduction of the oxide:

$$\mathrm{O}_{\mathrm{O}}^{\times} \rightleftharpoons \mathrm{v}_{\mathrm{O}}^{\bullet\bullet} + 2\mathrm{e}' + \frac{1}{2}\mathrm{O}_{2(\mathrm{g})}, \tag{6}$$

with equilibrium constant

$$K_{\mathrm{red}} = \frac{c_{\mathrm{v}} c_{\mathrm{e}}^2 \left(p\mathrm{O}_2\right)^{1/2}}{N_{\mathrm{v}} N_{\mathrm{Ce}}^2 \left(p\mathrm{O}_2^{\ominus}\right)^{1/2}} = \exp\left(\frac{\Delta S_{\mathrm{red}}}{k_{\mathrm{B}}}\right) \exp\left(\frac{-\Delta H_{\mathrm{red}}}{k_{\mathrm{B}} T}\right). \tag{7}$$

N_{v} and N_{Ce} are the volume densities of anion and cation sites in bulk ceria; $p\mathrm{O}_2^{\ominus}$ is a standard oxygen partial pressure of 1 atm. The values of $\Delta S_{\mathrm{red}} = 1.3 \times 10^{-3}\,\mathrm{eV\,K^{-1}}$ and $\Delta H_{\mathrm{red}} = 4.67\,\mathrm{eV}$ used in this study are taken from Tuller and Nowick.[36] For given T, $p\mathrm{O}_2$, and c_{a} one can solve Equations (5) and (7) simultaneously to obtain c_{v} and c_{e}.

3.2 | Grain-boundary chemistry

The increased resistance of GBs compared to that of bulk ceria is attributed solely to the presence of SCLs adjacent to the GB core. That is, all other possible contributions to the grain-boundary resistance, for example, from the GB core, are assumed to be negligible.[19,39] For our continuum-level simulations we consider a one-dimensional grain of length l^{gr}, with GBs at $x = 0$ and $x = l^{\mathrm{gr}}$. If we restrict the considerations to the three point defects

(oxygen vacancies, acceptor cations, and electrons), there is only one possible thermodynamic driving force for the formation of SCLs in which oxygen vacancies are strongly depleted: the difference in the standard chemical potential of oxygen vacancies between grain boundary and bulk has to be negative ($\Delta\mu_v^{\ominus} = \mu_v^{\ominus,gb} - \mu_v^{\ominus,b} < 0$). The other two possibilities to produce vacancy-depleted SCLs ($\Delta\mu_a^{\ominus} > 0$, $\Delta\mu_e^{\ominus} > 0$) force small amounts of defects out of the GB core and hence do not produce large effects.[40] We assume that $\Delta\mu_v^{\ominus}$ is independent of temperature and defect concentrations; we also assume that there are N_v^{gb} sites within the GB core (with $N_v^{gb} \ll N_v^{b}$) that are characterized by $\Delta\mu_v^{\ominus} < 0$. We are aware that the number of possible sites as well as the difference in standard chemical potentials depend on the structure of the GB, but we ignore such variations here. The segregation of the oxygen vacancies to the GB core leads, through charge carrier redistribution, to space-charge formation: depletion of the vacancies and accumulation of the electrons adjacent to the positively charged core.[40,41] The dopant cations display a constant concentration throughout the system if we consider the Mott–Schottky case, whereas they are in electrochemical equilibrium (accumulated in the SCLs) in the Gouy–Chapman case.

The concentration profiles of the mobile point defects across the grain are calculated by solving Poisson's equation:

$$\varepsilon_0\varepsilon_r \frac{d^2\phi(x)}{dx^2} = -\rho(x) \tag{8}$$

for our one-dimensional grain with relative dielectric permittivity of $\varepsilon_r = 35$. The space-charge density ρ is given by [*cf.* Equation (5)]:

$$\rho(x) = -ec_a(x) + 2ec_v(x) - ec_e(x). \tag{9}$$

In order to link the concentration profiles to the electrostatic potential, we assume that the electrochemical potentials of the mobile defects are constant throughout the system. To avoid unphysically high defect concentrations, we take the Fermi–Dirac form for the electrochemical potentials for both bulk and grain-boundary phases, namely:

$$\tilde{\mu}_v = \mu_v^{\ominus} + k_B T \ln\left[\frac{c_v(x)}{N_v - c_v(x)}\right] + 2e\phi(x) \tag{10}$$

$$\tilde{\mu}_e = \mu_e^{\ominus} + k_B T \ln\left[\frac{c_e(x)}{N_{Ce} - c_e(x) - c_a(x)}\right] - e\phi(x) \tag{11}$$

$$\tilde{\mu}_a = \mu_a^{\ominus} + k_B T \ln\left[\frac{c_a(x)}{N_{Ce} - c_e(x) - c_a(x)}\right] - e\phi(x). \tag{12}$$

For the acceptor dopants and the electrons, these forms take into account that acceptor cations and electron polarons share the same (cation) sublattice. We are aware that Equation (12), referring to an effective acceptor species (see Section 3.1), is a simplification, but the use of separate electrochemical potentials for Ca''_{Ce} and Y'_{Ce} introduces additional mathematical complexity and is therefore eschewed.

All continuum-level simulations were carried out with the Finite-Element-Method (FEM) code, COMSOL Multiphysics®, Ver. 5.3.

3.3 | Connecting $c_v(x)$ with σ^b/σ^t

We consider only the vacancies' contribution to the measured conductivity—for both bulk and grain boundary—under these oxidizing conditions and in this range of measurement temperatures. The bulk conductivity is unambiguously due to oxygen vacancies: taking the electron mobility from Tuller and Nowick[42] and the calculated bulk electron concentrations (see Section 3.1), one finds that the bulk electronic conductivity is more than three orders of magnitude lower than the measured bulk conductivity for all conditions we examined. For the grain boundary, the situation is more complicated. Because of vacancy depletion and electron accumulation within the SCLs, the local electronic conductivity $\sigma_e(x)$ may exceed the local ionic conductivity $\sigma_v(x)$ as the GB core is approached. An ionic current cannot be converted, however, into an electronic current within a crystal without a change in the crystal's composition; such a transition can only occur at an electrode. (In the transmission-line picture,[43] the electronic and ionic rails run in parallel, connected by a chemical capacitance.) C^{gb}, however, is consistent with the extension of SCLs (see Section 4.2), and hence this transition is assumed not to be evident. We are aware that Guo et al found the GB conductivity in CeO_2 at low dopant concentration and high temperatures to be dependent on oxygen partial pressure, and that they regarded such behavior as evidence of increased electronic conductivity arising from electron accumulation in the SCLs.[9] We provide later (in Section 4.4) a simpler, alternative explanation for the pO_2-dependent GB conductivity, by showing that a purely ionic GB conductivity already shows a pO_2-dependence under certain conditions.

The procedure for calculating at T_{meas} the spatial distribution of oxygen vacancies in the SCL, and thus σ^b/σ^t, consists of four steps. First, bulk concentrations of vacancies and electrons are calculated at T_{crit} for given c_a and pO_2. T_{crit}, it is remembered, is the lowest temperature at which the dopant cations are sufficiently mobile (at the given cooling rate) to achieve electrochemical equilibrium. Second, Poisson's equation is solved at T_{crit} for given N_v^{gb} and $\Delta\mu_v^{\ominus}$ with all three defects (acceptors, vacancies, and electrons) being mobile; the bulk defect concentrations were already calculated in the previous step, and the decrease in the bulk dopant concentration due to accumulation within the SCL is neglected for large grains. Third, bulk defect concentrations are calculated

at T_{meas} for the same pO_2 and c_a. Finally, Poisson's equation is solved, this time at T_{meas}: vacancies and electrons are mobile and attain electrochemical equilibrium, with the bulk values c_v and c_e calculated for T_{meas}; acceptor dopants are immobile and $c_a(x)$ is given by the frozen-in profile obtained at T_{crit} in the second step (Figure 2); N_v^{gb} and $\Delta\mu_v^{\ominus}$ remain constant. It is stressed that the thermodynamic treatment of the SCLs allows us not only to predict the defect profiles at T_{crit} (electrochemical equilibrium for all charge carriers) but it also allows us to predict defect profiles for the restricted equilibrium case [$c_a(x)$ is frozen-in]. In considering the restricted equilibrium one has to specify a boundary condition. There is no reason to assume that the space-charge potential remains constant, nor that the GB charge remains constant. Rather it is the thermodynamic driving force that remains constant.

In order to connect the defect distribution of the oxygen vacancies in the SCL to measured quantities, we write the local conductivity as the product of vacancies' mobility u_v, charge q_v and concentration c_v. Assuming that the vacancy mobility is constant across the grain, that is in the bulk and in the SCLs, and taking the additional resistance to be an excess quantity, we obtain an equation that lets us calculate from $c_v(x)$ the ratio of the bulk to total conductivity σ^b/σ^t according to:

$$\frac{\sigma^b}{\sigma^t} = \frac{2\sigma^b}{l^{gr}}\left(\int_0^{l^{gr}/2}\frac{1}{\sigma(x)}dx\right) = \frac{2c_v^b}{l^{gr}}\left(\int_0^{l^{gr}/2}\frac{1}{c_v(x)}dx\right). \quad (13)$$

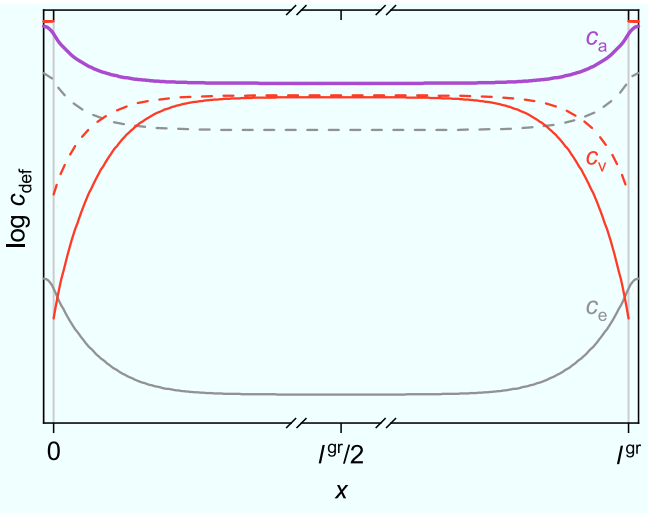

FIGURE 2 Point-defect concentrations of the dopants (purple), the oxygen vacancies (red), and the electrons (gray) in the SCL at the critical temperature T_{crit} (dashed lines) and at a temperature of the impedance spectroscopy measurements T_{meas} (solid lines) ($T_{meas} < T_{crit}$). The dopant profile is frozen-in at T_{crit} and not in equilibrium at T_{meas} (purple). The grain is framed by GB cores (interface marked with vertical gray lines) and is extended from 0 to l^{gr}

The integration is performed over half a grain from 0 to $l^{gr}/2$, since the system (bulk + GBs) is symmetrical about $l^{gr}/2$.

For the analytical description of the GB resistance the two extreme, simple cases, Mott–Schottky and Gouy–Chapman, are often used. The resulting ratios of the bulk to total conductivity can be expressed in terms of the Debye length $l_D = \sqrt{\frac{\varepsilon_0\varepsilon_r k_B T}{2e^2 c_a^b}}$, and the space-charge potential Φ_0.[19]

$$\left(\frac{\sigma^b}{\sigma^t}\right)_{MS} \approx \frac{2l_D}{l^{gr}}\frac{\exp\left(\frac{2e\Phi_0}{k_B T_{meas}}\right)}{\left(\frac{4e\Phi_0}{k_B T_{meas}}\right)^{1/2}} + 1 \quad (14)$$

$$\left(\frac{\sigma^b}{\sigma^t}\right)_{GC} \approx \frac{4l_D}{3l^{gr}}\exp\left(\frac{3e\Phi_0}{2k_B T_{meas}}\right) + 1 \quad (15)$$

4 | RESULTS AND DISCUSSION

4.1 | Microstructural analysis

In order to determine the grain size l^{gr}, we analyzed six scanning electron micrographs that contained in total over 800 grains (one such micrograph is shown in Figure 3). The analysis yielded an average grain size of 4.37 μm, which becomes through the correction factor an estimated 3D grain diameter of 6.99 μm. Image analysis also indicated that the darker regions in Figure 3 (we attribute them to porosity) represent ca. 5% of the total area; this value for the porosity is consistent with the Archimedes' result.

If Si is present in ceria powders, even in small amounts, a silica/silicate phase will form at the GBs upon sintering,[4,5] and this can be attributed to the low solubility of Si in CeO_2 (and other fluorite-structured oxides). As noted

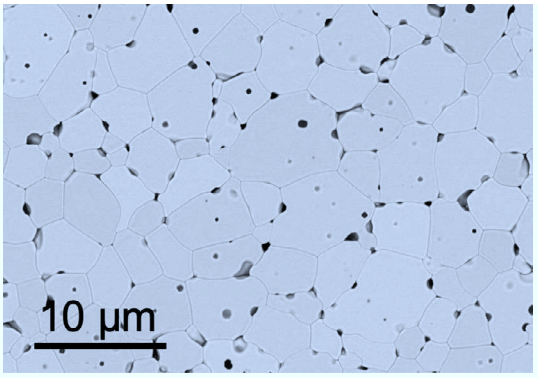

FIGURE 3 Scanning electron micrograph of a $Ce_{0.9985}Y_{0.0011}Ca_{0.0004}O_{1.99905}$ ceramic, sintered at T_{sint} = 1573 K, ground and polished, and then thermally etched at T = 1473 K. The area shown is 28 μm × 40 μm

in the Introduction, the presence of such GB phases also gives rise to a GB resistance. Here, in order to be able to apply the space-charge model, we need to be able to rule out the presence of such silica-based phases. Three GBs were studied with TEM and the micrographs do not give any indications for second phases (Figure 4). The elemental composition of the GBs and over the whole sample were checked. The Si impurities are within the error of EDXS measurement. A small amount of Al impurities distribute homogeneously over the whole sample. Therefore, a diminished GB conductivity can be attributed to the presence of SCL.

The HAADF image in Figure 5A shows two neighboring grains (bright contrast) together with their boundary area (dark contrast). The GB has been tilted to an edge-on condition and its width, estimated approximately from the full width at half maximum (FWHM) of the intensity profile of the HAADF image across this GB, is in the range of 1.0 to 1.5 nm. In Figure 5B the specimen was further tilted until both grains are close to zone axis. Under this condition, high-resolution STEM images that show atom columns were acquired. It can be seen that the neighboring grains are atomically connected and the GB is sharp. This was found to be a common feature based on our statistical measurements. By means of fast Fourier transform (FFT) analysis, it was determined that the normal direction of the two grains lies on their <211> axis. The interplanar distances are (3.18 ± 0.02) Å and (1.96 ± 0.02) Å for $\{1\bar{1}1\}$ and $\{02\bar{2}\}$ planes, respectively, which are consistent with the reported values (3.13 and 1.91 Å).[44] All of these observations show that the specimen consists of crystalline grains adopting the fluorite structure and no amorphous GB phases.

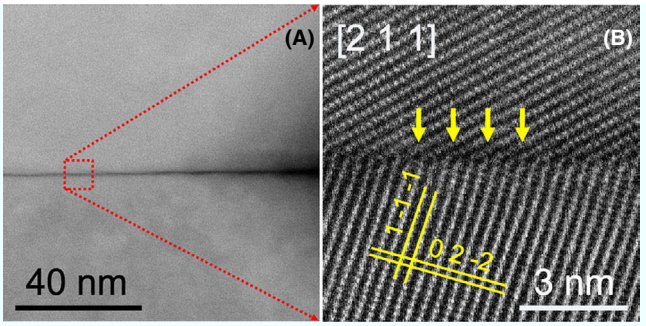

FIGURE 5 A, HAADF image over the area 100 nm × 100 nm showing the morphology of a typical GB, the specimen was tilted until both grains are viewed end-on. B, High-resolution STEM image of the area marked by the red square in the HAADF image (8.75 nm × 8.75 nm); The specimen was rotated until both grains are close to zone axis

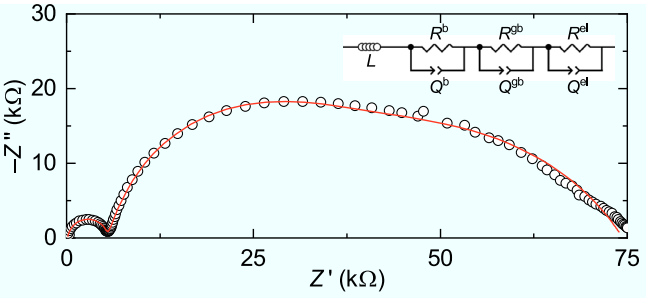

FIGURE 6 Electrochemical impedance spectrum of a $Ce_{0.9985}Y_{0.0011}Ca_{0.0004}O_{1.99905}$ ceramic obtained with Pt|Ag electrodes at T_{meas} = 783 K in air ($0.1 \le f/\text{Hz} \le 4 \times 10^7$)

4.2 | Impedance spectroscopy

A typical impedance spectrum obtained for a $Ce_{0.9985}Y_{0.0011}Ca_{0.0004}O_{1.99905}$ ceramic is shown in Figure 6. Bulk and GB resistances were extracted from each spectrum (the second arc consists of overlapping responses from the GBs and from the electrodes[45]) by fitting a conventional equivalent circuit $L\left(R^{b}Q^{b}\right)\left(R^{gb}Q^{gb}\right)\left(R^{el}Q^{el}\right)$ to the data.[46] Q is a constant phase element of impedance $Z = Q^{-1}(i\cdot\omega)^{-n}$; capacitances were calculated from R, Q, and n according to $C = \left(R^{1-n}Q\right)^{1/n}$.[47] An inductor L was included in order to take in account the signal from the physical inductance of the wires. The effects of inductances appeared at high frequency and became more obvious at high temperatures. The high-frequency arc can be ascribed to the bulk response since the corresponding capacitance is consistent with the value calculated from the bulk

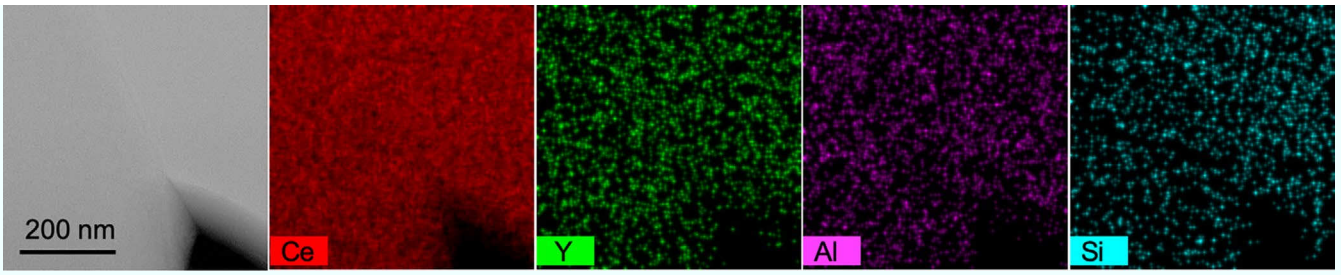

FIGURE 4 EDXS mapping of a GB, the images of Ce, Y, Si, and Al are shown in net counts and the shown area is 550 nm × 550 nm large. No increased concentrations of impurities in the GB can be detected

dielectric permittivity (C^b ~10 pF). The grain boundary capacitance is consistent with the presence of space-charge layers (C^{gb} ~10 nF). A more detailed analysis of C^{gb} will be given in a future publication.

Using Equations (1)-(3) we calculated from the extracted resistances and capacitances the bulk and GB conductivities. In Figure 7 we plot the conductivities as a function of inverse temperature: the GB conductivity is seen to be roughly three orders of magnitudes lower than the bulk conductivity. Figure 7 also shows a comparison of our conductivity data with literature data for Y-doped CeO_2 ceramics of similar, though not identical, Y content but converted to the same Y concentration.[9,48,49] The conductivities measured in this study fall in between the literature data. The activation enthalpy calculated here fits better to the one obtained by Guo et al.[9] Wang et al[48] and Faber et al[49] used the intersection of the arc with the real axis as the resistance of the bulk, whereas we and Guo et al obtained resistances by fitting the spectra with equivalent circuits. The simulated resistance is different from the intersection, because in the obtained spectra the centre of the arc is often depressed below the real axis.

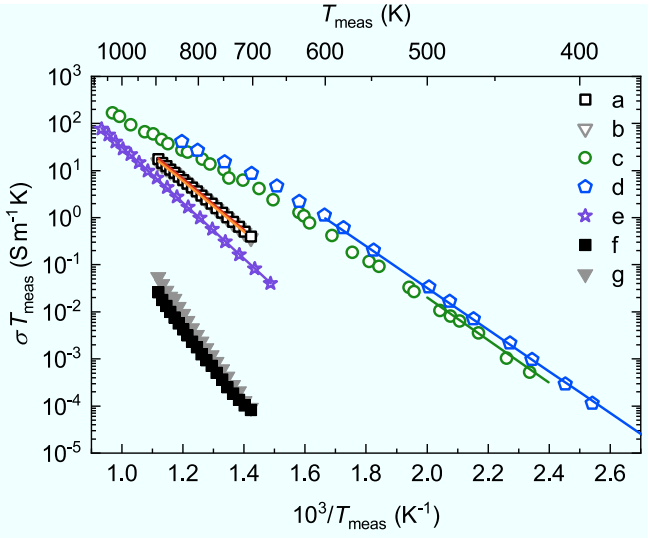

FIGURE 7 Comparison of bulk conductivity data for weakly doped CeO_2 as a function of reciprocal temperature T_{meas}. The original data refer to slightly different Y contents within the dilute regime, but the conductivities shown here were all converted to a common $c_a = 0.19$ mol%: (a) and (b) were measured in this study for $Ce_{0.9985}Y_{0.0011}Ca_{0.0004}O_{1.99905}$ with two equivalent samples (sample a: open squares and sample b: open triangles), (c) were measured by Wang et al[48] for $Ce_{0.999}Y_{0.001}O_{1.9995}$ (green dots), (d) by Faber et al[49] for $Ce_{0.999}Y_{0.001}O_{1.9995}$ (blue pentagons) and (e) by Guo et al[9] for $Ce_{0.998}Y_{0.002}O_{1.999}$ (purple stars). The GB conductivities measured in this study (f) and (g) is also plotted (sample a: filled squares and sample b: filled triangles). The lines show the Arrhenius fits for the determination of the activation enthalpy (a: $\Delta H^b_\sigma = 1.07$ eV, b: $\Delta H^b_\sigma = 1.06$ eV, c: $\Delta H^b_\sigma = 0.90$ eV[48], d: $\Delta H^b_\sigma = 0.88$ eV[49], e: $\Delta H^b_\sigma = 1.12$ eV[9])

4.3 | Ratio of the bulk to total conductivity: simulations and experiments

In order to predict σ^b/σ^t for the restricted-equilibrium case from the thermodynamic model, one has to specify, first, the critical temperature below which the dopant distribution is frozen in. This is difficult to estimate, partly because the exact temperature-time profile experienced by the ceramics is not known. Furthermore, the temperature distribution within the ceramic as a function of time is not known. Grain boundaries close to the surface may cool much faster than boundaries in the sample's center, giving rise to a variation in critical temperatures. We have taken a single critical temperature of $T_{crit} = 1273$ K, based on the furnace cooling rate from the sintering temperature, and cation diffusion data.[50] One also needs, of course, to specify the parameters characterizing the GB defect chemistry, N_v^{gb} and $\Delta\mu_v^{\ominus}$. These parameters depend on the GB structure, and hence, some substantial variation from GB to GB is expected. Here we use single values for each parameter, these values being effective over all boundaries probed in the impedance measurements.[51,52]

In Figure 8 we show that the conductivity ratio calculated with Equation (13) for two slightly different sets of GB parameters describes well the two sets of experimental data. The driving energies of $\Delta\mu_v^{\ominus} \approx -2$ eV are physically reasonable, in the sense that they represent the difference in two formation energies. The number of preferential sites for vacancies in the GB ($N_v^{gb} \approx 1.1 \times 10^{27}$ m^{-3}) is reasonable, too, as one expects $N_v^{gb} \ll N_v^b$. Given our incomplete knowledge of the sample's thermal history and the variation in GB properties, we do not expect to extract unique values.

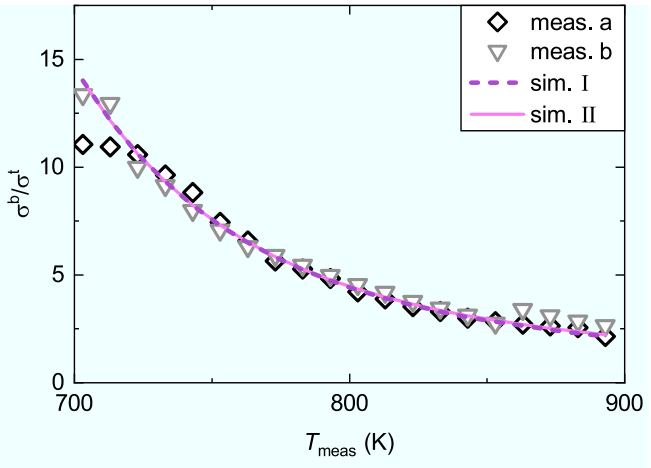

FIGURE 8 Ratio of the bulk to total conductivity σ^b/σ^t as a function of temperature T_{meas} for $Ce_{0.9985}Y_{0.0011}Ca_{0.0004}O_{1.99905}$ obtained by EIS from two measurements (open triangles and squares) in comparison to simulated conductivity data (dashed line I: $\Delta\mu_v^{\ominus} = -1.9$ eV, $N_v^{gb} = 1.1 \times 10^{27}$ m^{-3}, $T_{crit} = 1273$ K; solid line II: $\Delta\mu_v^{\ominus} = -2.0$ eV, $N_v^{gb} = 1.2 \times 10^{27}$ m^{-3}, $T_{crit} = 1273$ K)

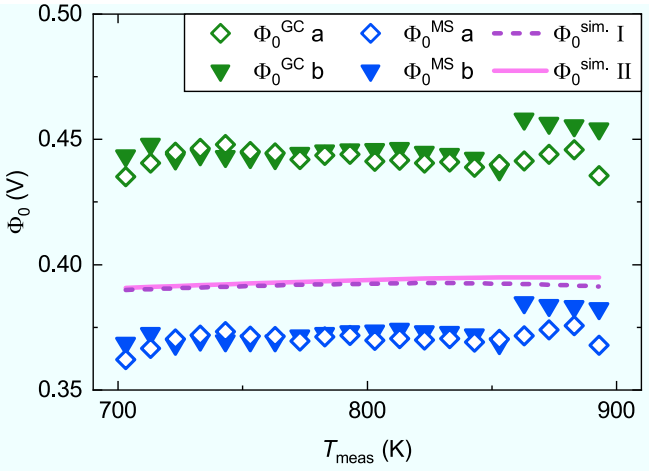

FIGURE 9 Calculated potential Φ_0 as a function of the temperature T_{meas}. The potential describes the experimental ratio of the bulk to total conductivity for two measurements (sample a and b) in terms of the theoretical description for the Mott–Schottky (MS, blue symbols) and Gouy–Chapman case (GC, green symbols) (Equations (14) and (15)). In comparison the simulated potential is shown for two space-charge parameter sets, where the dopant distribution at the critical and measurement temperature is taken into account (dashed line I: $\Delta\mu_v^{\ominus} = -1.9\,\text{eV}, N_v^{gb} = 1.1\times10^{27}\,\text{m}^{-3}, T_{crit} = 1273\,\text{K}$; solid line II: $\Delta\mu_v^{\ominus} = -2.0\,\text{eV}, N_v^{gb} = 1.2\times10^{27}\,\text{m}^{-3}, T_{crit} = 1273\,\text{K}$)

The standard (simple) method for obtaining the space-charge potential from conductivity data is to assume the Mott–Schottky or the Gouy–Chapman case. We recall that neither case is strictly applicable to our ceramics: In the Mott–Schottky case the accumulation of the dopants at the GBs at the high (sintering) temperature is ignored, and in the Gouy–Chapman case the frozen-in dopant profile at the measurement temperature is not taken into account. Nevertheless, it is important to see how well these simple cases describe the true behavior. In Figure 9 we compare our values of Φ_0 with those obtained by applying Equations (14) and (15) to experimental data. Our values lie between the two standard cases, and we hypothesize that the true potential in the restricted-equilibrium case will always lie between the two extremes. Further, extensive calculations are required, however, to support this hypothesis. In the present case, that is, for this acceptor concentration, this GB chemistry and this T_{crit}, it appears that the values from the Mott–Schottky analysis are closer to the real potential than those from the Gouy–Chapman analysis. For other samples and other materials, however, with different concentrations, with different GB chemistry and with different T_{crit}, the Gouy–Chapman analysis may be more appropriate. We recommend, therefore, analysis with both expressions.

4.4 | Why the GB conductivity may depend on oxygen partial pressure

Finally we return to the question of why the GB conductivity of weakly doped ceria can depend on oxygen partial pressure,[9] if only the transport of oxygen vacancies contributes to the measured conductivity. Specifically, we show in Figure 10 results for a more weakly doped composition ($Ce_{0.9995}Y_{0.0005}O_{1.99975}$), for which the effect is more pronounced, obtained from our restricted-equilibrium model as

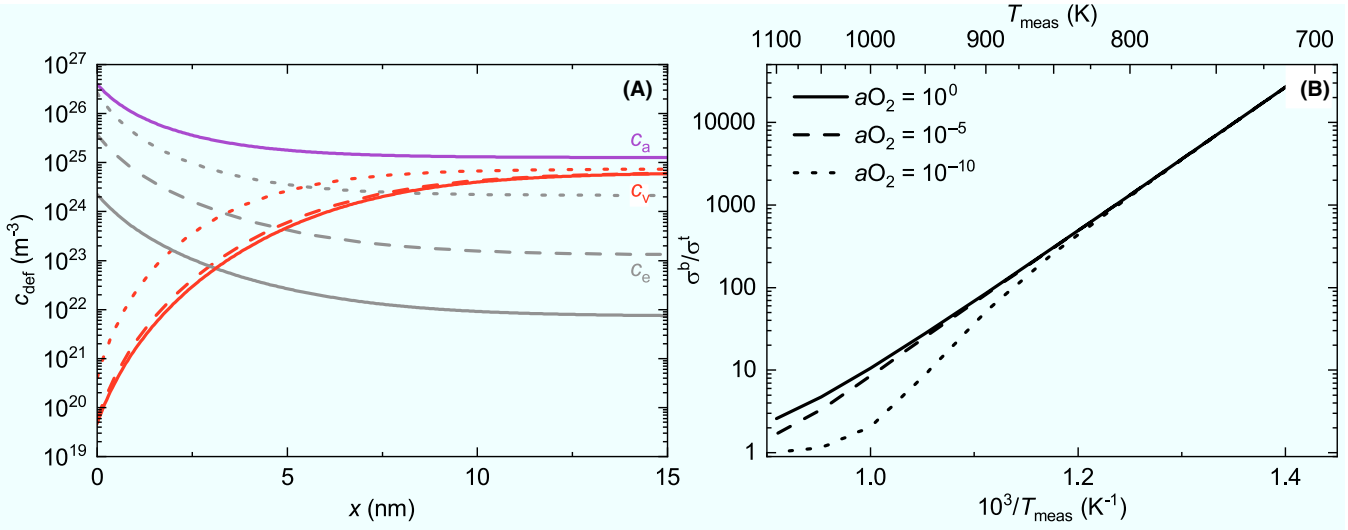

FIGURE 10 Oxygen-activity dependence of (A) the point-defect concentrations in the SCL and (B) the conductivity ratio σ^b/σ^t as a function of the reciprocal measurement temperature T_{meas} for CeO_2 with $c_a = 0.05$ mol%. The behavior is shown at three different atmospheres: $aO_2 = 10^0$ (solid lines), $aO_2 = 10^{-5}$ (dashed lines) and $aO_2 = 10^{-10}$ (dotted lines). With the restricted-equilibrium model the distribution of the oxygen vacancies (red), electrons (gray), and acceptor dopants (purple) at $T_{meas} = 1000$ K is calculated. The influence of the oxygen partial-pressure dependent electron concentration on the potential leads to pressure dependent ionic GB conductivities especially at high T_{meas}. (Used space-charge parameters $\Delta\mu_v^{\ominus} = -1.9\,\text{eV}, N_v^{gb} = 1.1\times10^{27}\,\text{m}^{-3}, T_{crit} = 1273\,\text{K}$)

a function of oxygen partial pressure. The bulk concentration of oxygen vacancies hardly varies with oxygen partial pressure (at this dopant concentration) but the bulk electron concentration increases (see Section 3.1). The increased electron concentration leads to higher electron concentration at the GBs, and in this way, to lower space-charge potentials. Consequently, the degree to which oxygen vacancies are depleted in the SCLs is far less, and the (ionic) GB conductivity rises. If we examine the conductivity ratio (Figure 10B), we see that the ratio is pO_2-independent at low temperatures but becomes increasing pO_2-dependent with increasing temperature. This is exactly the behavior observed by Guo et al.

These results show that it is important (a) to include the electrons in the bulk and at the GBs, even though they do not contribute to the measured (bulk and GB) conductivities; and (b) to perform modelling of the space-charge layers from the thermodynamic level of $\Delta\mu_v^{\ominus}$.

5 | CONCLUSIONS

The study of interfaces in oxides is a challenging subject because the problems are complex and interrelated. Here we have shown the benefits of attacking the problems with a variety of techniques. The TEM results revealed a polycrystalline ceramic with pristine GBs. EIS yielded the conductivities of the bulk and the grain boundaries, with the GB conductivity being roughly three orders of magnitudes lower than the bulk conductivity. In order to interpret the results, continuum-level simulations were performed. The four main results are:

1. The ratio of the bulk to total conductivity can be described by a restricted-equilibrium model, in which the dopant distribution is equilibrated at a high temperature but it is frozen in at the lower temperatures of the EIS measurements.
2. The comparison of measured and simulated conductivity data allows us to extract the thermodynamic driving force for space-charge formation.
3. For dilute solutions, the space-charge potential obtained from the more realistic case (restricted equilibrium) falls between those from Gouy–Chapman and Mott–Schottky cases.
4. The (ionic) GB conductivity may display a dependence on oxygen-partial pressure, if the electron concentration in the core is high enough to affect the GB charge and thus the space-charge potential.

ACKNOWLEDGMENTS

Funding by the German Research Foundation (DFG, Deutsche Forschungsgemeinschaft) is gratefully acknowledged within the Priority Programme (SPP) 1959/1 under grant numbers SO 499/9-1 (RWTH), GU 993/9-1 (IEK-1) and DU 1086/10-1 (ER-C/PGI-5). Discussions with Prof. Jürgen Fleig are gratefully acknowledged.

ORCID

Jana P. Parras https://orcid.org/0000-0001-8288-5495
Roger A. De Souza https://orcid.org/0000-0001-7721-4128

REFERENCES

1. Wang DY, Nowick AS. The "grain-boundary effect" in doped ceria solid electrolytes. J Solid State Chem. 1980;35(3):325–33.
2. El Adham K, Hammou A. "Grain boundary effect" on ceria based solid solutions. Solid State Ionics. 1983;9–10:905–12.
3. Gerhardt R, Nowick AS. Grain-boundary effect in ceria doped with trivalent cations: I, Electrical measurements. J Am Ceram Soc. 1986;69(9):641–6.
4. Gerhardt R, Nowick AS, Mochel ME, Dumler I. Grain-boundary effect in ceria doped with trivalent cations: II, Microstructure and microanalysis. J Am Ceram Soc. 1986;69(9):647–51.
5. Tanaka J, Baumard J-F, Abelard P. Nonlinear electrical properties of grain boundaries in an oxygen-ion conductor (CeO_2·Y_2O_3). J Am Ceram Soc. 1987;70(9):637–43.
6. Christie G, van Berkel F. Microstructure—ionic conductivity relationships in ceria-gadolinia electrolytes. Solid State Ionics. 1996;83(1–2):17–27.
7. Lee J-S, Kim D-Y. Space-charge concepts on grain boundary impedance of a high-purity yttria-stabilized tetragonal zirconia polycrystal. J Mater Res. 2001;16(9):2739–51.
8. Zhou X-D, Huebner W, Kosacki I, Anderson HU. Microstructure and grain-boundary effect on electrical properties of gadolinium-doped ceria. J Am Ceram Soc. 2002;85(7):1757–62.
9. Guo X, Sigle W, Maier J. Blocking grain boundaries in yttria-doped and undoped ceria ceramics of high purity. J Am Ceram Soc. 2003;86(1):77–87.
10. Heyne L. Interfacial effects in mass transport in ionic solids. In: Bénière F, Catlow C, editors. Mass transport in solids. New York, NY: Plenum Press, 1983: p. 425.
11. Tian C, Chan S-W. Ionic conductivities, sintering temperatures and microstructures of bulk ceramic CeO_2 doped with Y_2O_3. Solid State Ionics. 2000;134(1–2):89–102.
12. Tschöpe A. Grain size-dependent electrical conductivity of polycrystalline cerium oxide II: space charge model. Solid State Ionics. 2001;139(3–4):267–80.
13. Guo X, Waser R. Electrical properties of the grain boundaries of oxygen ion conductors: Acceptor-doped zirconia and ceria. Prog Mater Sci. 2006;51(2):151–210.
14. Grieshammer S, Grope B, Koettgen J, Martin M. A combined DFT + U and Monte Carlo study on rare earth doped ceria. Phys Chem Chem Phys. 2014;16(21):9974–86.
15. Žguns PA, Ruban AV, Skorodumova NV. Ordering and phase separation in Gd-doped ceria: a combined DFT, cluster expansion and Monte Carlo study. Phys Chem Chem Phys. 2017;19(39):26606–20.
16. Žguns PA, Ruban AV, Skorodumova NV. Phase diagram and oxygen-vacancy ordering in the CeO_2-Gd_2O_3 system: a theoretical study. Phys Chem Chem Phys. 2018;20(17):11805–18.

17. Koettgen J, Grieshammer S, Hein P, Grope B, Nakayama M, Martin M. Understanding the ionic conductivity maximum in doped ceria: trapping and blocking. Phys Chem Chem Phys. 2018;20(21):14291–321.
18. Mebane DS, De Souza RA. A generalised space-charge theory for extended defects in oxygen-ion conducting electrolytes: from dilute to concentrated solid solutions. Energy Environ Sci. 2015;8(10):2935–40.
19. Tong X, Mebane DS, De Souza RA. Analysing the grain-boundary resistance of oxide-ion conducting electrolytes: Poisson-Cahn vs Poisson-Boltzmann theories. J Am Ceram Soc. 2019;1–18. https://doi.org/10.1111/jace.16716
20. Avila-Paredes HJ, Choi K, Chen C-T, Kim S. Dopant-concentration dependence of grain-boundary conductivity in ceria: a space-charge analysis. J Mater Chem. 2009;19(27):4837–42.
21. Sánchez-Bautista C, Dos Santos-García AJ, Peña-Martínez J, Canales-Vázquez J. The grain boundary effect on dysprosium doped ceria. Solid State Ionics. 2010;181(37–38):1665–73.
22. Yan D, Liu X, Bai X, Pei L, Zheng M, Zhu C, et al. Electrical properties of grain boundaries and size effects in samarium-doped ceria. J Power Sources. 2010;195(19):6486–90.
23. Yeh TC, Perry NH, Mason TO. Nanograin composite model studies of nanocrystalline gadolinia-doped ceria. J Am Ceram Soc. 2011;94(4):1073–8.
24. Yan PF, Mori T, Suzuki A, Auchterlonie GJ, Zou J, Drennan J. Grain boundary's conductivity in heavily yttrium doped ceria. Solid State Ionics. 2012;222–223:31–7.
25. Tanaka R, Oliveira WS, Brandão A, Abrantes J, Frade JR. Grain boundary conductivity of heterogeneous ceria gadolinia. Electrochim Acta. 2012;85:116–21.
26. Kim SK, Khodorov S, Lubomirsky I, Kim S. A linear diffusion model for ion current across blocking grain boundaries in oxygen-ion and proton conductors. Phys Chem Chem Phys. 2014;16(28):14961–8.
27. Van Laethem D, Deconinck J, Depla D, Hubin A. Finite element modelling of the ionic conductivity of acceptor doped ceria. J Eur Ceram Soc. 2016;36(8):1983–94.
28. Baral AK, Tsur Y. Impedance spectroscopy of Gd-doped ceria analyzed by genetic programming (ISGP) method. Solid State Ionics. 2017;304:145–9.
29. Van Laethem D, Deconinck J, Hubin A. Ionic conductivity of space charge layers in acceptor doped ceria. J Eur Ceram Soc. 2019;39(2–3):432–41.
30. Gerlt A, Criner AK, Semiatin L, Payton EJ. On the grain size proportionality constants calculated in M.I. Mendelson's "Average grain size in polycrystalline ceramics". J Am Ceram Soc. 2019;102(1):37–41.
31. Steele B, Floyd JM. Oxygen self-diffusion and electrical transport properties of nonstoichiometric ceria and ceria solid solutions. Proc Br Ceram Soc. 1971;19:55–76.
32. Ban Y, Nowick AS. Defects and mass transport in reduced cerium dioxide single crystals. Proc 5th MaterialsRes Symp, Nat Bur Stand Spec Publ.1972;(364).
33. Takahashi T. Solid electrolyte fuel cells (Theoretics and experiments). In: Hladik J, editor. Physics of electrolytes. London and New York: Academic Press, 1972: p. 989.
34. Ray SP, Nowick AS, Cox DE. X-ray and neutron diffraction study of intermediate phases in nonstoichiometric cerium dioxide. J Solid State Chem. 1975;15(4):344–51.
35. Tuller HL, Nowick AS. Doped ceria as a solid oxide electrolyte. J Electrochem Soc. 1975;122(2):255–9.
36. Tuller HL, Nowick AS. Defect structure and electrical properties of nonstoichiometric CeO_2 single crystals. J Electrochem Soc. 1979;126(2):209–17.
37. Zacherle T, Schriever A, De Souza RA, Martin M. Ab initio analysis of the defect structure of ceria. Phys Rev B. 2013;87(13):134104.
38. Beschnitt S, Zacherle T, De Souza RA. Computational study of cation diffusion in ceria. J Phys Chem C. 2015;119(49):27307–15.
39. Kim S, Kim SK, Khodorov S, Maier J, Lubomirsky I. On determining the height of the potential barrier at grain boundaries in ion-conducting oxides. Phys Chem Chem Phys. 2016;18(4):3023–31.
40. De Souza RA. The formation of equilibrium space-charge zones at grain boundaries in the perovskite oxide $SrTiO_3$. Phys Chem Chem Phys. 2009;11(43):9939–69.
41. Tschöpe A, Kilassonia S, Birringer R. The grain boundary effect in heavily doped cerium oxide. Solid State Ionics. 2004;173(1–4):57–61.
42. Tuller HL, Nowick AS. Small polaron electron transport in reduced CeO_2 single crystals. J Phys Chem Solids. 1977;38(8):859–67.
43. Jamnik J. Impedance spectroscopy of mixed conductors with semi-blocking boundaries. Solid State Ionics. 2003;157(1–4):19–28.
44. Itoh T, Mori M, Inukai M, Nitani H, Yamamoto T, Miyanaga T, et al. Effect of annealing on crystal and local structures of doped zirconia using experimental and computational methods. J Phys Chem C. 2015;119(16):8447–58.
45. Haile SM, Staneff G, Ryu KH. Non-stoichiometry, grain boundary transport and chemical stability of proton conducting perovskites. J Mater Sci. 2001;36(5):1149–60.
46. Bauerle JE. Study of solid electrolyte polarization by a complex admittance method. Solid State Commun. 1969;7(15):2657–70.
47. Barsoukov E. Special aspects of impedance. In: Barsoukov E, Macdonald JR, editors. Impedance spectroscopy: theory, experiment, and applications, 2nd edn. Hoboken, New Jersey: John Wiley & Sons, Inc., 2005; p. 495.
48. Wang DY, Park DS, Griffith J, Nowick AS. Oxygen-ion conductivity and defect interactions in yttria-doped ceria. Solid State Ionics. 1981;2:95–105.
49. Faber J, Geoffroy C, Roux A, Sylvestre A, Abélard P. A systematic investigation of the dc electrical conductivity of rare-earth doped ceria. Appl Phys A. 1989;49:225–32.
50. Beschnitt S, De Souza RA. Impurity diffusion of Hf and Zr in Gd-doped CeO_2. Solid State Ionics. 2017;305:23–9.
51. Fleig J, Maier J. A finite element study on the grain boundary impedance of different microstructures. J Electrochem Soc. 1998;145(6):2081–9.
52. Fleig J. The influence of non-ideal microstructures on the analysis of grain boundary impedances. Solid State Ionics. 2000;131(1–2):117–27.

How to cite this article: Parras JP, Cao C, Ma Z, et al. The grain-boundary resistance of CeO_2 ceramics: A combined microscopy-spectroscopy-simulation study of a dilute solution. *J Am Ceram Soc*. 2020;103:1755–1764. https://doi.org/10.1111/jace.16843